Field Cycling Imaging: a novel modality to characterise breast cancer at low and ultra-low magnetic fields below 0.2T

Vasiliki Mallikourti
University of Aberdeen
Peter Ross
University of Aberdeen
Oliver Maier
Institute of Biomedical Imaging
Katie Hanna
University of Aberdeen
Ehab Hussein
NHG Grampians
Gareth Davies
University of Aberdeen
David Lurie
University of Aberdeen https://orcid.org/0000-0002-6009-3152
Gerald Lip
NHS Grampian https://orcid.org/0000-0002-7867-5468
Hana Lahrech
University of Aberdeen
Yazan Masannat
University of Aberdeen https://orcid.org/0000-0002-5895-5059
Lionel Broche
l.broche@abdn.ac.uk
University of Aberdeen https://orcid.org/0000-0002-8452-9838

Article

Keywords:

Posted Date: February 5th, 2024

DOI: https://doi.org/10.21203/rs.3.rs-3759270/v1

Additional Declarations: There is **NO** Competing Interest.

Version of Record: A version of this preprint was published at Communications Medicine on October 30th, 2024. See the published version at https://doi.org/10.1038/s43856-024-00644-2.

Abstract

We propose Field-Cycling Imaging (FCI), a new MRI technology accessing a range of low and ultra-low magnetic fields (2mT to 0.2T), to acquire longitudinal relaxation time over 4 orders of magnitude of field strength, and covering the whole body. FCI obtains the Nuclear Magnetic Relaxation Dispersion (NMRD) profiles of tissues, which probes molecular dynamics at micro- to nanometer scales. We present a prospective study including 10 female patients with breast cancers. Low magnetic fields clearly differentiate tumours from adipose and glandular tissues and discriminates true tumour extent beyond that of conventional imaging, matching the true pathological size of the lesion. Using our FCI prototype, T_1 variations at low and ultra-low field discriminate invasive from non-invasive cancers in patients ($p < 0.05$). To our knowledge, we described the first application of *in vivo* FCI in breast cancer, demonstrating relevant biomarkers that complement diagnosis of current imaging modalities, non-invasively and without contrast agents.

Introduction

Medical imaging is essential to assist physicians in patient management, diagnosis, follow-up, screening and in therapeutic decision-making. Most exploit the properties of penetrative electromagnetic radiation, with different modalities associated with different energy levels: X-rays for computer tomography (CT) scans and mammograms (MG), gamma rays for single-photon emission computerized tomography (SPECT), positron emission tomography (PET) scans, radiofrequency (RF) waves coupled to a magnetic field for magnetic resonance imaging (MRI) and sound waves in ultrasound (US) scanning. Each has its specific use in patient management. In particular, MRI benefits from the good tissue penetration of RF waves and does not affect the integrity of cells or biomolecules, allowing visualisation of the whole organ non-invasively. MR-based techniques therefore have a high potential for clinics and offer many sources of anatomical and functional tissue contrast mechanisms[1], especially when combined with contrast agents, although it is not a widespread imaging choice for the breast due to its high examination cost and limited accessibility.

Low-field MRI systems are showing a renewed interest as they offer solutions for more accessible devices. Low magnetic fields have been known for a long time to offer excellent endogenous T_1 contrast between tissues[2–4]), but very little is known about these contrast mechanisms below 0.2 T. This is largely due to the difficulty to obtain clinically usable images using magnetic fields in the mT range and below, where SNR strongly limits the technical possibilities. Yet, many technologies are emerging that aim precisely to explore that range, using various approaches[5].

Our approach is to explore these field regimes by using the technology of Fast-Field-Cycling Nuclear Magnetic Resonance (FFC-NMR). FFC-NMR is a long-established technique that employs rapidly varying magnetic fields with the aim to increase signal sensitivity by polarizing the spin magnetization at the highest available magnetic field strength (the polarisation field, B_0^P) before exploring interactions at a lower magnetic field (the evolution field, B_0^E). NMR signals are then measured by returning to a relatively high field (the detection field, B_0^D) where the Larmor frequency corresponds to that of the instrument's RF coil (see Fig. 2). This allows measuring the longitudinal relaxation times T_1 of proton spins over a large range of low magnetic fields using the same device, noninvasively. The output is a curve known as the T_1 Nuclear Magnetic Resonance Dispersion (NMRD) profile, which shows the field-dependence of the longitudinal relaxation T_1 (or more often the longitudinal relaxation rate $1/T_1$ NMRD).

Crucially, NMRD profiles report T_1 relaxation of water and are therefore quantitative informers of the molecular dynamics of water, but also of their neighbouring biomolecules such as proteins and lipids, spanning a time range that encompasses a large variety of water motions. It informs on the translational and rotational movements of their chemical groups, at the micro and nano-scales[6–10]. In particular, cellular transmembrane water exchange mechanisms affects T_1 at low and ultra-low magnetic fields and have been demonstrated to be a hallmark of cancer aggressiveness in breast cancer cell lines[11] and in invasion/migration in brain cancer tissues[12,13]. Furthermore, T_1 at low and ultra-low magnetic fields was found to correlate with hypoxia, H_2O_2 oxidative stress, and to the expression of aquaporins (water channel proteins that facilitate transmembrane water transport)[12]. All these results confirm pioneering works that showed potential applications of NMR at low and ultra-low magnetic fields in cancer[14], as well as later *ex vivo* and *in vivo* results demonstrating physiological[13] and pathophysiological mechanisms[12,15] that affect relaxation in cancer processes, indicating a high potential for FFC-NMR as a relevant technology for diagnostic and therapy follow-up, in particular in oncology.

Interestingly, NMRD profiles of living tissues may also exhibit a series of features called quadrupolar peaks (QP) in the $R_1 = 1/T_1$ profile (or dips if one observes the T_1 profile), visible around 65 mT, which are due to the cross-relaxation between water protons (^1H) and the N-terminal nitrogen (^{14}N) of slow-moving proteins[16,17]. QP cross-relaxations provide subtle information about protein dynamics and aggregation, and

their changes can reflect some pathophysiological mechanisms such as seen in cartilage[18,19] or blood serum[20], and more interestingly in cancer such as in sarcoma[21], breast[22] and brain[12].

Commercial FFC-NMR systems are available but can only analyse small specimens[23], or small animals with limited localisation[11]. Our research group has built a new prototype imager called Field-Cycling Imaging (FCI, formerly FFC-MRI), which is derived from MRI but exploits FFC-NMR to access T_1 contrast mechanisms over a very broad magnetic field strength from 20 μT to 200 mT, corresponding to proton Larmor frequency spectrum, from 850 Hz to 8.5 MHz. In addition to use rapidly switched magnets, FCI technology includes magnetic field gradients, corrective shims, and low-frequency RF coils with dedicated pulse sequences to produce images with new contrasts derived from NMRD profiles. Each image voxel therefore informs on the molecular dynamics of tissues and organs, with imaging capability over the entire body[24]. In this work we have used our FCI prototype to study patients with breast cancer for the first time to our knowledge. We demonstrate the potential of FCI to generate relevant biomarkers for breast cancer, to provide new diagnostic information.

The standard procedure for breast cancer imaging includes MG, considered as a gold standard for early detection of breast cancer, often supplemented by US scans. Both have limitations: MG is influenced by breast density while US is characterised by high false-positive rates. MRI is used in selected cases, especially in lobular pathology, mammographically occult lesions, dense breast tissue, screening for high-risk patient/gene carriers, and monitoring of treatment in Neoadjuvant Chemotherapy (NACT) while PET scans can assess the spread of cancer cells. Hybrid technologies such as PET/MRI or PET/CT systems[25] have been proposed to improve cancer detection and target specific cell functions by using suitable radiopharmaceutical contrast agent, while contrast-enhanced mammography (CEM), which uses iodinated contrast materials, and contrast-enhanced MRI, with gadolinium-based contrast agents, locate areas with high angiogenesis and assess vessel permeability[26], both being correlated to cancer malignancy.

Nevertheless, some types of breast pathologies remain difficult to detect on MRI images and, even if detected, MRI can underestimate the extent of the disease, particularly in margin areas with infiltrative cancer cells. The use of paramagnetic contrast agents is also required for MRI breast scans and there has been concern about gadolinium deposition in tissues[27]. Nevertheless, triple assessment remains the mainstay in assessing patients with breast complaints, and is a combination of clinical assessment, imaging and histology diagnosis from biopsy[28].

The aims of this study were (i) to demonstrate the performance of our FCI prototype[24] in a clinical trial, (ii) to investigate its potential contribution to the standard imaging in breast cancer diagnosis by comparing with other works at low and ultra-low fields using *ex vivo*[22] and *in vivo* preclinical cancer breast models[13], and (iii) to find quantitative FCI and low-field biomarkers related to the type of breast cancer pathology.

Materials and Methods

Patients

This prospective study was approved by the North of Scotland Research Ethics committee (study 19/NS/0064) and all participants gave written informed consent. Twenty-six females with breast cancer were recruited from January 2019 to March 2020 and from April 2021 to March 2022 by the Breast Unit at Aberdeen Royal Infirmary. The study design is shown in Fig. 1 and patient demographics in Table 1.

Table 1

Demographics of the study volunteers and tumour size as defined by each imaging modality. The size of the lesion is reported in mm (longest tumour size). ADCIS: apocrine ductal carcinoma in situ; DCIS: ductal carcinoma in situ; EPC: Encysted papillary carcinoma, IDC: invasive ductal carcinoma; ILC: invasive lobular carcinoma; IPLC: pleomorphic invasive lobular carcinoma; PDCIS: papillary ductal carcinoma in situ; Bord: borderline; BIRADs: Breast Imaging-Reporting and Data System used to define mammographic density. MG: mammography; NAD: no abnormality detected; US: ultrasound.

ID	Age (years)	Lesion type	Grade	Invasiveness	Tumour size measurement					
					BIRADs	HE Hist. (mm)	MG (mm)	US (mm)	MRI (mm)	FCI (mm)
P1	49	DCIS	High	Non-invasive	C	51	80	NAD	-	43
P2	70	ILC	2	Invasive	A	19	24	17	17	13
P2		DCIS	High	Non-invasive		43	NAD	NAD	NAD	39
P3	41	IDC/DCIS	3/High	Invasive	B	29	25	24	-	35
P4	56	PDCIS/EPC	Intermediate	Non-invasive	C	25	41	28	-	30
P5	44	ADCIS	High	Non-invasive	B	59	25	11	55	49
P6	50	IPLC/ILC/DCIS	2/High	Invasive	A	52	20	20	64	62
P7	65	DCIS	High	Non-invasive	B	36	26	NAD	42	42
P8	66	DCIS	High	Non-invasive	B	32	22	12	-	31
P9	45	Phyllodes	Bord.	-	D	30	26	37	-	39
P10	48	IDC	3	Invasive	B	36	33	25	-	32
Mean ±SD	53 ± 10									
Median(IQR)						36(29–51)	26(24–35)	22(13–27)	49(23–62)	39(31–43)

Among the 26 patients recruited, 7 did not complete the scan due to claustrophobia (n = 4) or technical issues (n = 3), one patient was excluded because of having chemotherapy before the scan and in 8 patients the breast lesion was small and had not been correctly localised within the single-slice FCI scan. Finally, 10 patients (from P1 to P10) have been successfully examined by FCI.

P2 presented two distinct lesions at histology (invasive lobular carcinoma (ILC) core surrounded by a ductal carcinoma in situ (DCIS) peripheral lesion). Each lesion was treated separately for the analysis. All patients had a clinical MG and US scan and four patients (P2, P5, P6 and P7) had additionally a clinically indicated 1.5T MRI scan using a T_2-FLAIR, diffusion-weighted imaging, pre-post dynamic contrast-enhanced and T_1-weighted contrast-enhanced sequences (Gadovist 1.0 mmol).

Routine Hematoxylin Eosin (HE) histology was conducted at the excised lesion after surgery as per standard practice to provide lesion phenotype, grade, and size as reported in Table 1.

Breast density was scored in BIRADs (Breast Imaging Reporting and Data System) categories from A (no dense breast) to D (extremely dense breast) by an experienced consultant breast radiologist (co-author GL) (Table 1).

FCI acquisition

Details of the FCI scanner have been previously published[24]. A dedicated RF coil was designed to image both breasts simultaneously (Fig. 2, b and c) at 193 mT (8.2 MHz). The FCI scans were performed before surgery in prone position, using an inversion recovery spin echo sequence with echo time of 16 ms and four evolution fields (200, 65.8, 22 and 2.3 mT) chosen to report on two different relaxation behaviors below and above 22 mT, previously observed *ex vivo* in another FCI study (data not published) on normal breast imaging, and at 65.8 mT to assess the amplitude of QPs relaxation. T_1 was evaluated using five evolution times at each field (Fig. 4a). No contrast agents were used.

The imaging size parameters were adapted to each patient, the FOV was set between 300 to 500 mm with an image size of 64 x 128 and in-plane spatial resolution of 2 to 4 mm. Acquisitions were realised on only one axial slice with 10 mm thickness positioned at the level of the lesion, due to technical limitations of our prototype FCI scanner. No signal averaging was performed. The total scan duration was 45 minutes including calibrations, axial and sagittal navigator images and FCI images.

Data analysis

The raw FCI images were processed using MATLAB 2019a (The MathWorks, Inc., Natick, Massachusetts, United States) to remove artefacts[29] and by tailor-made TGV-based software written in Python to obtain T_1 maps[30]. Three Regions-of-Interest (ROIs) were manually drawn on the FCI scans of contralateral breasts to select adipose and glandular tissue and on abnormal breast to select the lesion as shown in Fig. 3. Notice that positions of ROIs were validated by an experienced (> 10 years) consultant breast radiologist (co-author GL), based on results from MG, US, and MRI (when available). P7 had a partial mastectomy before recruitment, therefore healthy tissue ROI in adipose was selected from the abnormal breast while glandular tissue was not clearly seen.

The ROIs were used to average the magnetization from the FCI images and to obtain the $1/T_1$ NMRD profiles from curve fitting (details in Supplement, Eq. 1). The NMRD profiles of the different tissues were then fitted (see Supplement, Eq. 2) to derive the dispersion (β parameter) of the NMRD profile at fields below (β_L) and above (β_H) 22 mT. The amplitude of the QPs peaks at 65.8 mT was estimated by subtracting the baseline provided from interpolation.

Tumour sizes in FCI images were calculated using ImageJ[31], and measured as per standard procedures for other imaging modalities. In MRI, the 2nd dynamic post contrast acquisition was used as per standard procedures. The longest dimension is reported (Table 1). All tumour size measurements obtained from a given imaging modality, were compared to HE histology using the ratio in %: $(A_{IM} - A_{HE})/A_{HE}) \times 100$, where A_{IM} corresponds to tumour area of a given imaging modality and A_{HE} to the tumour area of HE histology.

The Signal-to-Noise Ratio (SNR) was measured at each field on the magnitude FCI image acquired at the longest evolution time, with one ROI positioned on the contralateral healthy breast and the other on the image background, using the Rayleigh correction factor[32] (Supplement, Eq. 3). The Contrast-to-Noise Ratio (CNR) was measured from the same FCI images using the ROIs from tumour and adjacent healthy tissues (Supplement, Eq. 4). The differences in T_1 between tumour and adjacent healthy tissue, referred to as tumour-to-background contrast ratio, were calculated as the differences from the corresponding ROIs in T_1 maps and are provided in percent of average T_1 ($\%\Delta T_1$, Supplement, Eq. 5). All these methodological specifications are reported in Table 2.

Table 2
SNR and CNR from magnitude FCI images, and %ΔT1 from T1 maps, calculated between tumours and adjacent uninvolved breast tissue at different field strengths B0E. The values are presented as median, minimum, and maximum values across all patients.

$B_0{}^E$	200 mT		65.8 mT		22 mT		2.3 mT	
	Median	Range	Median	Range	Median	Range	Median	Range
SNR	58	27–101	29	9–58	16	3.5–26	4.5	2.2–9
CNR	26	8–67	10	3.5–38	9	3.5–18	3.4	0.4–7.8
$\%\Delta T_1$	31	-14–65	32	10–89	60	29–116	55	23–109

Statistical analyses were performed using SPSS Statistics 28 (IBM corp., Chicago, United States). Tumour size and FCI biomarkers comparisons were made using Mann Whitney U tests, with Wilcoxon signed rank tests when comparing signals between tissues using differences within each patient. A p-value below 0.05 was considered statistically significant.

Data are given as median values with interquartile range in parenthesis. Values were visualised using boxplots; on each box, the central line indicates the median, and the bottom and top edges of the box indicate the 25th and 75th percentiles, respectively. The whiskers, bottom and top, indicate the minimum and maximum, respectively.

Data availability

This study is recorded on www.researchregistry.com under UIN number 4875.

The data that support the finding of this study are available from the corresponding author upon reasonable request.

The TGV software developed to analyse the FCI images is also available under the Apache license v2.0 (https://github.com/IMTtugraz/PyQMRI).

Results

FCI images

For all patients, the tumour region was easily visible (see SNR and CNR values in Table 2) and the tumour-to-background contrast ratio (%ΔT_1) was more pronounced at lower fields (median [range]%: 31 [-14–65]% at 200 mT and 55 [23–109]% at 2.3 mT, with maximum value at 22 mT: 60 [29–116]%). At this 22 mT, the corresponding FCI images and T_1 maps clearly discriminate tumours from glandular and from adipose tissues, as shown in Fig. 3 for different tumour types.

Typical FCI data are shown in Fig. 4 (patient P2), including FCI images and T_1 maps for the four magnetic fields we have used (Figs. 4a and b, respectively). Magnetization relaxations recovery of the tumour region are shown in Fig. 4c and exhibit a monoexponential behavior for the four fields, but we cannot exclude a biexponential behavior if using a finer evolution time sampling for smaller values of t^E, as reported in other work[13]. Figure 4d shows the $1/T_1$-NMRD profiles extracted from images of P2 over homogeneous ROIs of the DCIS, glandular and adipose tissues, with the largest T_1 variations observed in breast tissues (86 to 175 ms). Qualitative differences appear at first sight in the dispersion profiles, which can be measured quantitatively on the T_1 values between tumour tissues and normal breast.

Tumour size estimation

summarises the tumour size measurements obtained by all imaging modalities for all the patients. There was no statistically significant bias in the lesion size measured from FCI at ultra-low field (in particular at 22 mT) compared to HE histology (39 [31–43] mm vs 36 [29–51] mm with Z =-0.22, p-value > 0.5, equal to 0.8 from Wilcoxon singed rank test), highlighting the performance of FCI to delineate whole tumour *in vivo*, despite the limitation from single-slice imaging. For the other imaging modalities, 2 out of 8 DCIS cases were severely under-estimated by US and/or MG, and one DCIS case was over-estimated by MG (P1). FCI did not miss any of the 11 cases. For the other imaging modalities, 3 out of 8 DCIS cases were not detected by US and/or MG and one DCIS case was not detected by MRI (P2). Typical Images (US, MG, MRI and FCI) from P2 and P5 are presented in Fig. 5a, showing the regions corresponding to the tumour (as indicated by arrows), but larger in FCI than detected by MG and US. For P2, US, MG, and MRI detect only the invasive core (ILC, ROIs in blue), not showing the surrounding DCIS area. FCI detects both the invasive core (hyperintense area indicated by blue arrow) and the surrounding DCIS area (hypointense area indicated by red arrow), with different contrast levels. For P5, US and MG underestimates the size of the DCIS (as indicated by ROIs and arrows in white) while DCIS was detected retrospectively in MG. Figure 5b shows the tumour sizes as measured from each imaging modality compared to HE histology, along with the NAD (no abnormality detected) cases, where each point shows the estimation of the tumour size from MG (grey), US (yellow), MRI (red) and FCI (blue). Size measurements by FCI (at 22 mT) were close to the histological reference, while those from MG and US were more scattered. Figure 5c shows the tumour size deviations as measured from each imaging modality referenced to HE histology. The FCI size deviations were very low (less than 3%), confirming the accuracy of FCI in evaluating the whole tumour area non-invasively.

FCI NMRD profiles and biomarkers for breast cancer detection

Figure 6a shows the corresponding $1/T_1$-NMRD profiles of three ROIs selected: in the tumour, in non-involved adipose tissues, and in non-involved glandular tissues. All the NMRD curves exhibited a general $1/T_1$ decrease with the magnetic field strength, with a variation of a factor 2 to 5 between 200 and 2.3 mT depending on the tissue types. More interestingly, $1/T_1$ values from tumours were significantly lower than adipose and glandular tissues at all fields, (or conversely T_1 was longer), except at 2.3 mT where $1/T_1$ from tumours did not significantly differ from glandular tissues (Fig. 6b-e, Table 3). The low-field dispersion β_L appeared significantly larger in tumours (0.12 [0.03–0.2]) compared with adipose tissues (0.06 [0.05–0.08]). Relaxation rate enhancements at 65.8 mT, which results from the ^{14}N-^{1}H quadrupolar coupling (arrow indicated on Fig. 6a), appear larger in tumours (0.9 [0.6–1.1] s^{-1}) compared with glandular tissues (0.8 [0.5–0.9] s^{-1}). Note that no QP signal was detected in adipose tissue (Fig. 6a and f), as expected from tissues with low protein content. This also agrees with *ex vivo* experiments[22], indicating that QP relaxation can be used to improve breast tumour detection. The model parameters extracted from the data are summarised in Table with their significance levels, including QP relaxation enhancements, showing that β_L and A_{QP} are candidate biomarkers of molecular dynamics for the detection of breast cancer against breast tissues.

Table 3
$1/T_1$ values and parameters derived from the power law mathematical model: β parameter at high-field (β_H) and low-field (β_L) and QP peak amplitudes (A_{QP}). All data are given as median and interquartile range in parenthesis. p-values were derived by Wilcoxon signed rank tests between tumour and glandular tissues and tumour and adipose tissues.

	Tumour	Glandular tissue	Adipose tissue	Tumour vs glandular		Tumour vs adipose	
				Z	p-value	Z	p-value
$1/T_{1\ 200mT}$ (s^{-1})	4.4 (2.3–6.5)	5.7 (5.0–6.0)	7.3 (7.0–7.7)	-2.2	0.028	-2.9	0.003
$1/T_{1\ 65.8mT}$ (s^{-1})	6.6 (3.1–8.0)	7.4 (5.8–8.3)	8.3 (8.0–8.4)	-2.2	0.028	-2.9	0.003
$1/T_{1\ 22mT}$ (s^{-1})	6.6 (3.4–7.8)	8.0 (5.3–9.0)	9.0 (8.9–10.2)	-2.8	0.005	-2.8	0.004
$1/T_{1\ 2.3mT}$ (s^{-1})	8.1 (6.8–10.3)	10.1 (8.1–11.6)	11.0 (9.9–11.9)	-1.8	0.074	-2.8	0.004
β_H	0.14 (0.04–0.23)	0.19 (0.08–0.22)	0.10 (0.07–0.16)	-0.26	0.799	-0.98	0.328
β_L	0.12 (0.03–0.21)	0.11 (0.09–0.15)	0.06 (0.05–0.08)	-1.2	0.241	-2.0	0.041
A_{QP} (s^{-1})	0.9 (0.6–1.1)	0.8 (0.5–0.9)	0.15 (-0.4–0.25)	-0.6	0.575	-2.5	0.013

FCI biomarkers of breast cancer invasion

The $1/T_1$ NMRD profiles from breast tumours showed some variability between patients, and further categorisation of these profiles according to tumour invasiveness showed significant differences between invasive and non-invasive tumours (Fig. 7a). These appeared in the dispersion parameter β (0.19 [0.09–0.26] in non-invasive vs 0.05 [0.03–0.09] in invasive tumours, Z = -2.1, p = 0.038, Fig. 7). The $1/T_1$ relaxation rate at 2.3 mT was markedly higher in non-invasive tumours, although not significantly (9.9 [8.0–10.9] s^{-1} in non-invasive against 7.1 [3.8–7.9] s^{-1} in invasive, Z = -1.9, p = 0.067, Fig. 7c). These differences in tissue relaxation time T_1 also appeared clearly within patient P2, where the tumour core appeared brighter (high invasion phenotype, higher T_1) and was surrounded by the darker DCIS (non-invasive region, lower T_1), from 2.3 mT to 65.8 mT (see Fig. 4b). These agree with the literature, supporting the claim that T_1 relaxation at ultra-low fields in living tissues is a relevant biomarker discriminating invasion from non-invasion. This phenomenon is linked to the transmembrane water exchange, which has been found to be more rapid in tissues with glioma cells invasion[12,33]. Also, QP peak amplitudes were markedly higher for non-invasive tumours, although not significantly (0.9 [0.7–1.8] s^{-1} in non-invasive vs 0.5 [0.06–1.0] s^{-1} in invasive, Z = -1.5, p = 0.171, Fig. 7d Fig. 7). One can also note that the trend followed by the tumour dispersion profiles below 2.3 mT suggests that larger tissue contrast can be observed at lower fields, potentially providing even greater discrimination between tissues, with more powerful tests for the detection of breast tumour invasiveness.

HE Histology confirmed if tumours were invasive or not. Figure 7e-f shows typical HE histology images for non-invasive DCIS (P8) and invasive IDC (P10) respectively. $1/T_1$ NMRD profiles from these two cases are shown in Fig. 7g depicting the different dispersions (β = 0.15 in non-invasive vs 0.04 in invasive), which supports the role of molecular dynamics as relevant biomarkers to discriminate tumour invasion from non-invasion.

Discussion

This study was a first step in determining the clinical effectiveness of FCI and its unique advantage over existing diagnostic techniques. We have shown for the first time that NMRD profiles can be extracted from FCI images *in vivo* from breast cancer patients, providing clinically relevant and complementary information without the need for contrast agents. The image quality of our FCI prototype was sufficient to generate accurate T_1 maps and NMRD profiles, and the tissue contrast accurately discriminated the lesions from non-involved tissues. T_1 maps at 22 mT provided non-biased size estimates validated by histology, despite the technical limitation to image a single slice by FCI. The narrow bore (50 cm diameter) made patient recruitment challenging but FCI scans are quiet and relatively comfortable.

Interestingly, FCI assessed tumour size more accurately than MG and US on average and, contrary to MG, did not present issues with breast density despite the range of BIRADs scores. Indeed, the dispersion levels were significantly different between lipidic and tumour tissues. Also, FCI did not present false negatives, contrary to US and MG imaging. If confirmed, this could be a major asset in dense breasts, especially when scanning young patients. The mixed lesion from P2 was also significantly under-estimated by US, MG, and MRI as confirmed from

histology, yet FCI could detect the two regions separately and provided a more precise measurement of the DCIS part than other imaging modalities. This illustrates an important issue with breast imaging, where some types of breast cancers remain difficult to detect and under-estimations may lead to repeated operations due to involved margins for the patients that have breast conserving surgery, while overestimation may lead to unnecessary mastectomies. This includes missing lobular cancer due to its discohesive and infiltrative nature, subtle calcifications, and breast density which both lead to biases in tumours diagnosis. From this study, it appears that FCI can overcome some of these limitations and have a complementary role in the estimation of tumour size, including involved margins.

The shape of NMRD profiles successfully discriminated between tumours, adipose and glandular tissues, and its dispersion discriminated between invasive and non-invasive tumours, including IDC, ILC, and DCIS, resulting from the changes in the molecular dynamics of water.

The QP peaks amplitude was also slightly lower in invasive tumours compared with non-invasive ones, although the dispersion of the $1/T_1$ – NMRD profiles was a more significant discriminator. Consequently, QP relaxation may not be a biomarker of breast cancer in isolation but may be combined with the other FCI signals to provide more accurate measurement of tumour invasiveness and spread, with applications in efficient surgery guiding and potential impact in treatment planning.

Additionally, the results obtained agree with preclinical FFC-NMR studies of cancer mouse models *ex vivo* and *in vivo*, which showed a causal relationship between the T_1 increase (or $1/T_1$ decrease) in tumours at low fields (typically below 50 mT) and the increase of transmembrane water exchanges driven by the increased cell metabolism in invasive tumours[12,15,33]. We can thereby highlight the major role that FCI could have as a diagnostic imaging modality to specifically monitor drug efficiencies that modulate some cancer processes such as hypoxia, H_2O_2 oxidative stress, and aquaporin expressions.

The prototype scanner used in this study is the first ever to be used for clinical studies and has therefore several important limitations. Its narrow bore, single-slice scans and limited SNR and CNR made it challenging to recruit patients, to detect the whole tumour and to find small lesions, but our results clearly demonstrated the potential that this technology has in breast cancer. A faster, wider-bore FCI system is currently under construction in a clinical setting to start a larger study which will address these limitations, bringing this technology closer to the clinic. While this study focuses on breast cancer, our on-going work shows that B_0-dependent biomarkers appear across other pathologies, particularly in cancers. The potential for imaging without contrast agents is also a great benefit as it simplifies the examination, eliminates the need for Gadolinium-based contrast agents where there is concern about Gadolinium deposition[27], and allows regular MRI screening of women at higher risk of breast cancer, e.g. BRCA gene carriers.

More broadly, FCI can inform on fixed-field MRI measurements at set magnetic field strengths selected to highlight the best contrast levels for a specific disease or pathophysiological process. For instance, our results suggest that the contrast between tumours and healthy tissues is better perceived at 22mT, while contrast between invasion and non-invasion regions are better targeted at 2.3mT (Fig. 7g).

To conclude, FCI shows high potential for breast tumour detection with accurate delineation and provides unique insights about water dynamics in cancer at the micro and nanoscale. This offers new contrast sources that inform on pathophysiological processes in breast cancer, including invasive and non-invasive phenotypes, and helps to better define their extent. This may impact breast cancer diagnosis since the detection of invasion and migration processes remain challenging by current medical imaging modalities.

Abbreviations

FFC-NMR: Fast Field-Cycling Nuclear Magnetic Resonance

FCI: Field Cycling Imaging

NMRD: Nuclear Magnetic Resonance Dispersion

QP: Quadrupolar

RF: RadioFrequency

SNR: Signal to Noise Ratio

CNR: Contrast to Noise Ratio

DCIS: Ductal Carcinoma in Situ

ILC: Invasive Lobular Carcinoma

HE: Hematoxylin and Eosin

US: UltraSound

MG: MammoGraphy

NAD: No Abnormality Detected

Declarations

Competing interests

The authors have no relevant competing interests to declare.

Materials & Correspondence

Requests for material and correspondence should be sent to LMB.

Funding

This project has received funding from the European Union's Horizon 2020 research and innovation program under grant agreement No 668119 (project "IDentIFY"), as well as from the NHS Grampian Endowment Trust.

Author contributions

V.M. performed patient scans, conducted data and statistical analysis, constructed the figures, contributed to the writing of the manuscript; J.R. contributed to the construction and testing of the breast coil, pulse sequence development, conducted patient scans; O.M. conducted TGV analysis; K.H. participated to statistical analysis; E.H. performed histopathological analysis; G.D. contributed to the construction and testing of the breast radiofrequency coil; H.L. contributed to the funding, contributed to data interpretation, figure preparation, writing and review of the manuscript; G.L. performed radiological assessment; D.L. contributed to the conceptualisation and funding of the project, and to the review of the manuscript; Y.M. performed patient recruitment, secured the funding, designed the study, interpreted results and reviewed the manuscript; L.B. contributed to the funding, protocol design, supervision and conduct of FCI measurements and data analysis, writing of the paper, and review of the manuscript.

Acknowledgements

The authors would like to thank radiographers Nichola Crouch, Mike Hendry, Laura Reid, Michelle Mauchline, and Arthur Ginsburg for their support with patient scans of FCI, Stacey Dawson for the study coordination, and the clinical teams of the Royal Aberdeen Infirmary for their support, in particular Sue Rodwell, Lorraine Drage, Farah Muir, Vera Hord and Dr Mairi Fuller for their help with patient recruitment.

References

1. Campana, A., Gandomkar, Z., Giannotti, N. & Reed, W. The use of radiomics in magnetic resonance imaging for the pre-treatment characterisation of breast cancers: A scoping review. Journal of Medical Radiation Sciences 70, 462–478 (2023).
2. Damadian, R. Tumor Detection by Nuclear Magnetic Resonance. Science 171, 1151–1153 (1971).
3. Hazlewood, C. F., Chang, D. C., Medina, D., Cleveland, G. & Nichols, B. L. Distinction between the Preneoplastic and Neoplastic State of Murine Mammary Glands. *Proceedings of the National Academy of Sciences* 69, 1478–1480 (1972).
4. Mallard, J., Hutchison, J. M. S., Edelstein, W., Ling, R. & Foster, M. Imaging by nuclear magnetic resonance and its bio-medical implications. Journal of Biomedical Engineering 1, 153–160 (1979).
5. Sarracanie, M. & Salameh, N. Low-Field MRI: How Low Can We Go? A Fresh View on an Old Debate. Front. Phys. 8, (2020).
6. Abragam, A. *Principles of Nuclear Magnetism*. (Oxford University Press, 1983).
7. Kimmich, R. Molecular Dynamics in Polymers. in *Principles of Soft-Matter Dynamics* 373–498 (Springer Netherlands, 2012).

8. Kimmich, R. *Field-cycling NMR Relaxometry*. (The Royal Society of Chemistry, 2018). doi:10.1039/9781788012966.
9. Kruk, D. *Understanding Spin Dynamics*. (Pan Stanford, 2015). doi:10.1201/b19179.
10. Rössler, E. A., Stapf, S. & Fatkullin, N. Recent NMR investigations on molecular dynamics of polymer melts in bulk and in confinement. Current Opinion in Colloid & Interface Science 18, 173–182 (2013).
11. Ruggiero, M. R. *et al.* Evidence for the Role of Intracellular Water Lifetime as a Tumour Biomarker Obtained by In Vivo Field-Cycling Relaxometry. Angew Chem Int Ed Engl 57, 7468–7472 (2018).
12. Petit, M. *et al.* Fast-field-cycling NMR at very low magnetic fields: water molecular dynamic biomarkers of glioma cell invasion and migration. NMR in Biomedicine 35, e4677 (2022).
13. Ruggiero, M. R. *et al.* Evidence for the Role of Intracellular Water Lifetime as a Tumour Biomarker Obtained by In Vivo Field-Cycling Relaxometry. Angewandte Chemie International Edition 57, 7468–7472 (2018).
14. Koenig, S. H. & Brown III, R. D. Field-cycling relaxometry of protein solutions and tissue: Implications for MRI. Progress in Nuclear Magnetic Resonance Spectroscopy 22, 487–567 (1990).
15. Ruggiero, M. R. *et al.* Intracellular Water Lifetime as a Tumor Biomarker to Monitor Doxorubicin Treatment via FFC-Relaxometry in a Breast Cancer Model. Front Oncol 11, 778823 (2021).
16. Jiao, X. & Bryant, R. G. Noninvasive measurement of protein concentration. Magn Reson Med 35, 159–161 (1996).
17. Voigt, G. & Kimmich, R. Quadrupolar dip in proton relaxation dispersion of poly(vinyl chloride). *Journal of Magnetic Resonance (*1969*)* 24, 149–154 (1976).
18. Broche, L. M., Ashcroft, G. P. & Lurie, D. J. Detection of osteoarthritis in knee and hip joints by fast field-cycling NMR. Magn Reson Med 68, 358–362 (2012).
19. Petrov, O. V. & Stapf, S. Multicomponent analysis of T1 relaxation in bovine articular cartilage at low magnetic fields. Magnetic Resonance in Medicine 0, (2018).
20. Wang, Z. *et al.* Detection of Metabolite–Protein Interactions in Complex Biological Samples by High-Resolution Relaxometry: Toward Interactomics by NMR. J. Am. Chem. Soc. 143, 9393–9404 (2021).
21. Masiewicz, E. *et al.* Towards applying NMR relaxometry as a diagnostic tool for bone and soft tissue sarcomas: a pilot study. Sci Rep 10, 14207 (2020).
22. Di Gregorio, E., Ferrauto, G., Lanzardo, S., Gianolio, E. & Aime, S. Use of FCC-NMRD relaxometry for early detection and characterization of ex-vivo murine breast cancer. Sci Rep 9, 4624 (2019).
23. Ferrante, G. & Sykora, S. TECHNICAL ASPECTS OF FAST FIELD CYCLING. in *Advances in Inorganic Chemistry* vol. 57 405–470 (Academic Press, 2005).
24. Broche, L. M., Ross, P. J., Davies, G. R., MacLeod, M.-J. & Lurie, D. J. A whole-body Fast Field-Cycling scanner for clinical molecular imaging studies. Sci Rep 9, 10402 (2019).
25. Hatazawa, J. The Clinical Value of Breast Specific Gamma Imaging and Positron Imaging: An Update. Seminars in Nuclear Medicine 52, 619–627 (2022).
26. Sardanelli, F., Fausto, A., Menicagli, L. & Esseridou, A. Breast vascular mapping obtained with contrast-enhanced MR imaging: implications for cancer diagnosis, treatment, and risk stratification. Eur Radiol Suppl 17, 48–51 (2007).
27. Neal, C. H. Screening Breast MRI and Gadolinium Deposition: Cause for Concern? Journal of Breast Imaging 4, 10–18 (2022).
28. Willett, A., Mitchell, M. & Lee, M. *Best Practice Diagnostic Guidelines for Patients Presenting with Breast Symptoms*. (2010).
29. Broche, L. M., Ross, P. J., Davies, G. R. & Lurie, D. J. Simple algorithm for the correction of MRI image artefacts due to random phase fluctuations. Magnetic Resonance Imaging 44, 55–59 (2017).
30. Bödenler, M. *et al.* Joint multi-field T1 quantification for fast field-cycling MRI. Magnetic Resonance in Medicine 86, 2049–2063 (2021).
31. Schneider, C. A., Rasband, W. S. & Eliceiri, K. W. NIH Image to ImageJ: 25 years of image analysis. Nat Methods 9, 671–675 (2012).
32. Firbank, M. J., Coulthard, A., Harrison, R. M. & Williams, E. D. A comparison of two methods for measuring the signal to noise ratio on MR images. Phys. Med. Biol. 44, N261 (1999).
33. Ruggiero, M. R. *et al.* Role of Transmembrane Water Exchange in Glioma Invasion/Migration: In Vivo Preclinical Study by Relaxometry at Very Low Magnetic Field. Cancers 14, 4180 (2022).

Figures

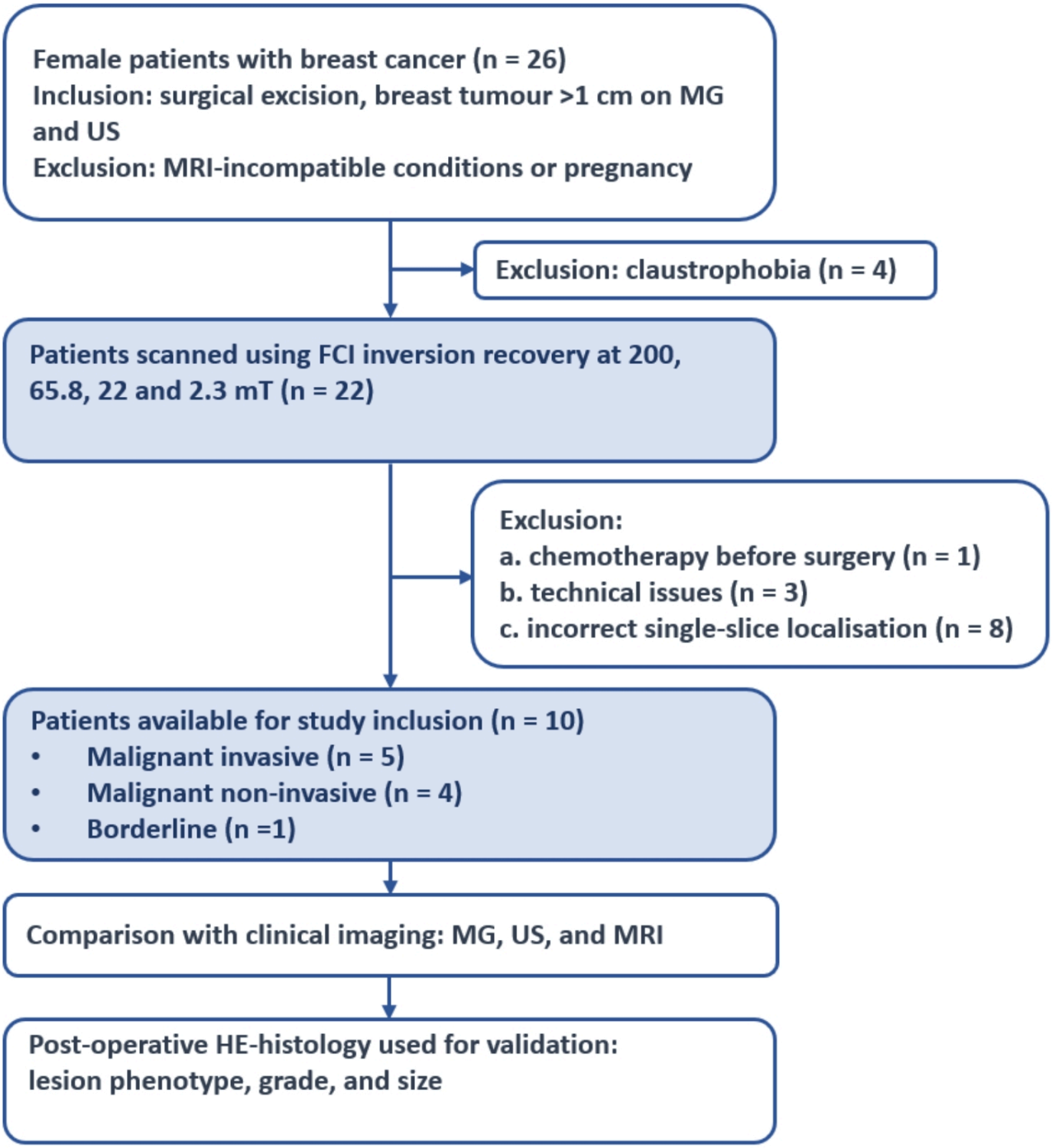

Figure 1

Flow diagram of the clinical protocol of patients undergoing FCI, including the criteria of patient inclusion and exclusion, the patient groups related to the cancer nature, the imaging modalities, and the standard post-operative histology analysis.

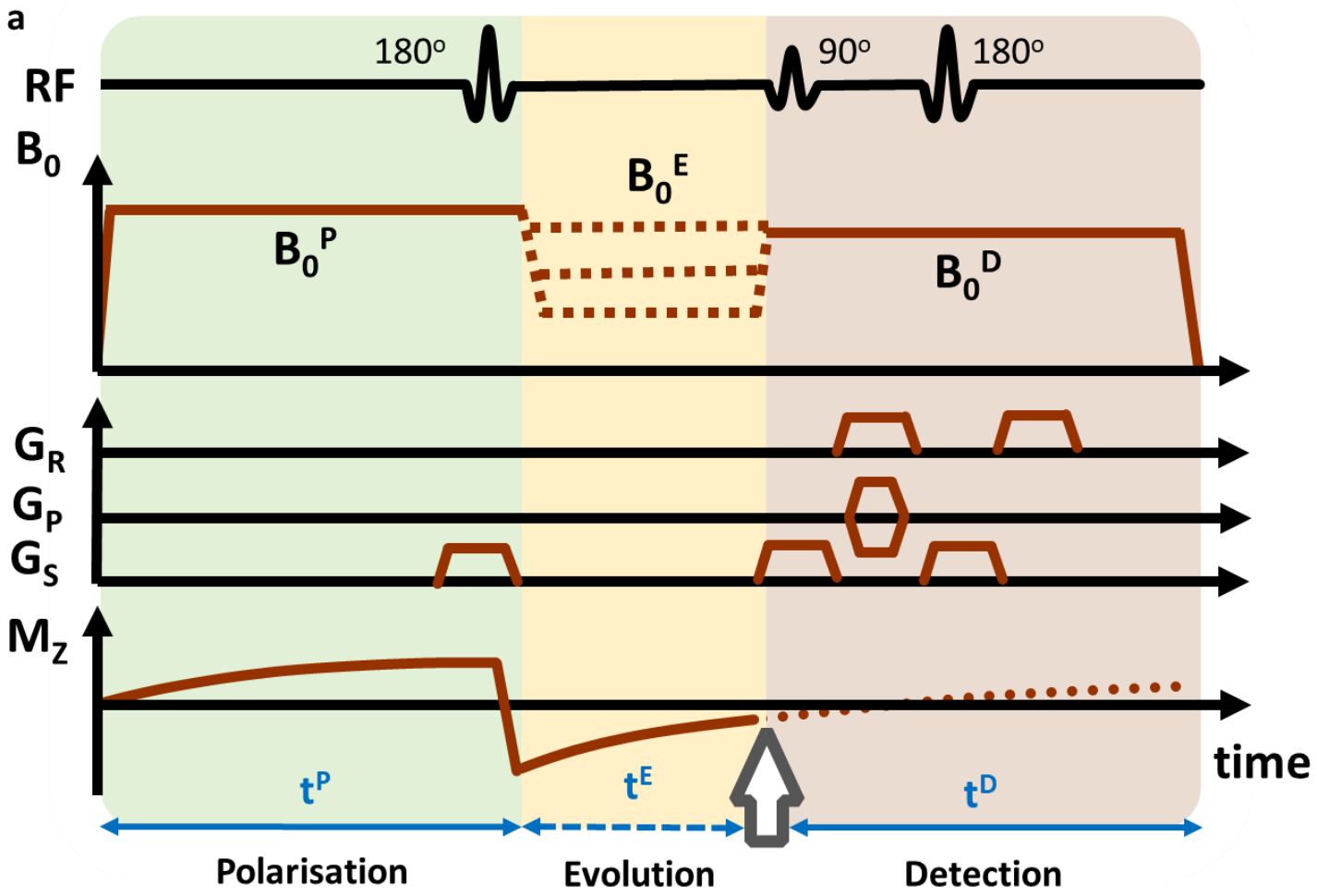

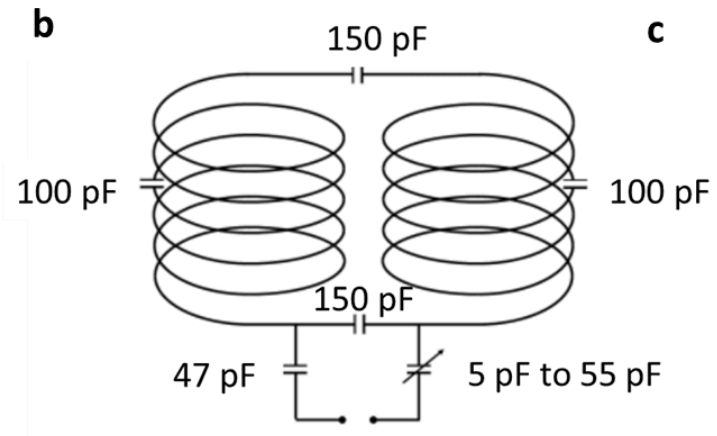

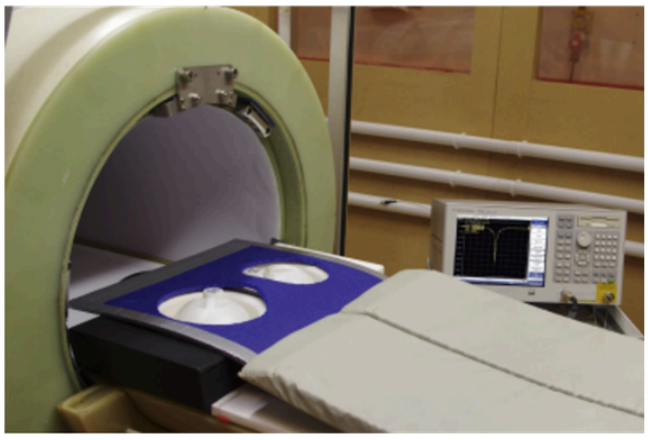

Figure 2

FCI sequence and breast coil. a) Diagram of FCI sequence combining the inversion recovery spin echo with typical gradient echo acquisition using magnetic gradients G_R, G_P and G_S for, read, phase and slice encoding, respectively. Mz is the longitudinal magnetization and its polarization is done at the highest field (here at 0.2T during 300 ms). Signal detection is also performed at a higher field, here at 193 mT, which Larmor proton frequency corresponds to the RF coil frequency. During acquisitions, the magnetic field is switched rapidly between the polarization (B_0^P), evolution (B_0^E) and detection (B_0^D) stages to ensure good SNR. Measurements are performed with varying B_0^E (illustrated by red dashed lines) and the whole process is repeated with different evolution times (t^E) to measure T_1 relaxation (illustrated by blue dashed line). At the end we obtain the T_1- NMRD profiles (T_1 versus B_0^E). **b)** Schematic of our home-made bilateral breast coil circuit, with a

resonance frequency at 8.2 MHz for signal detection at 193 mT. The coil design was selected to provide a simple and robust transmit/receive coil with good field uniformity and as much volume as could be provided in the limitations imposed by the bore/couch rail geometry. The selected capacitor distribution was to prevent excessive voltage between any sections of the coil and to ensure that the path of the RF pulse in the coil never exceeded $1/10^{th}$ of a wavelength. The loaded quality factor of the RF coil was 120, demonstrating its good performance. **c)** Picture of the FCI prototype scanner used, with the breast coil in place and loaded with two phantom bottles.

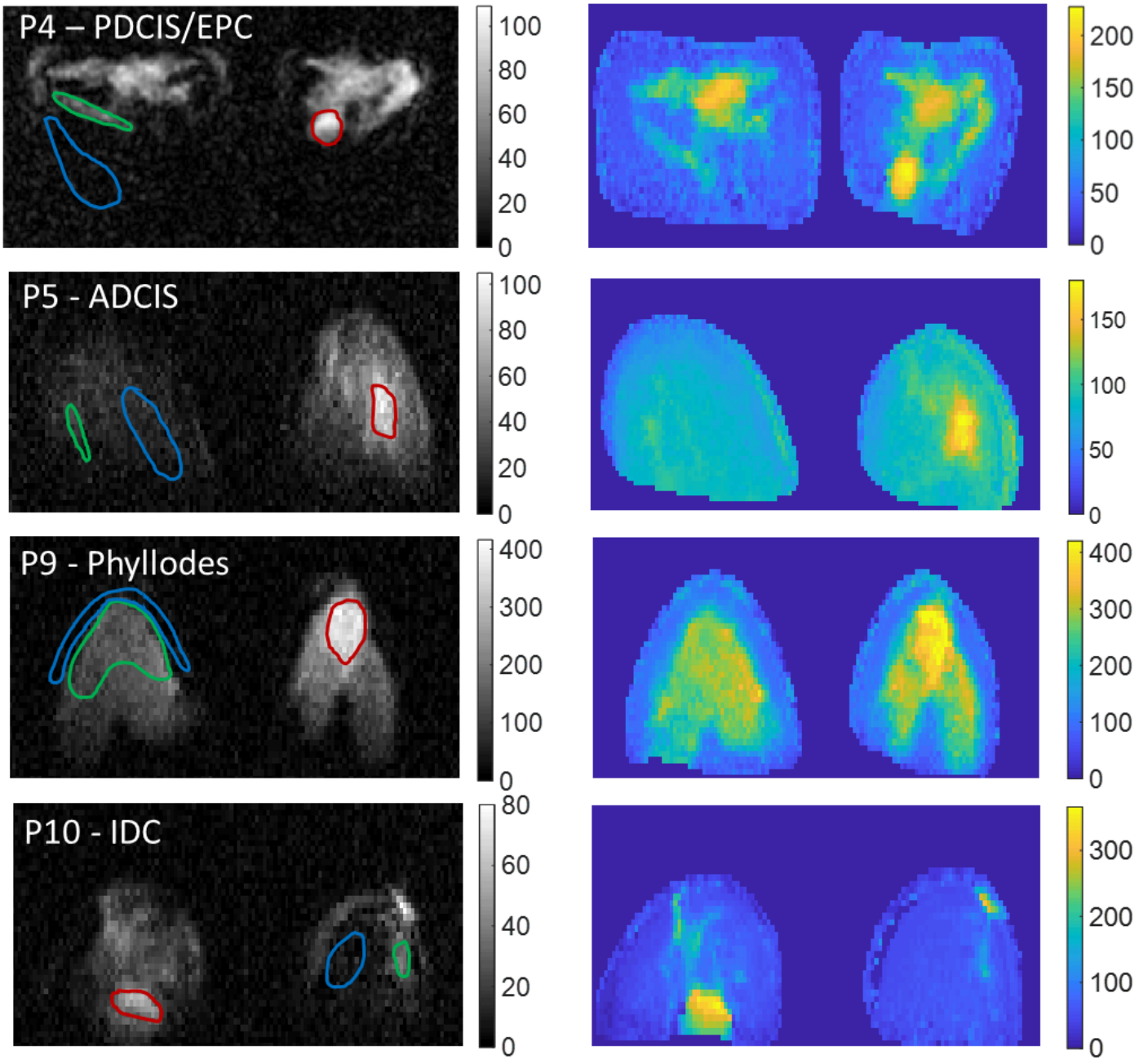

Figure 3

Typical FCI axial magnitude images at 22 mT and t^E of 88 ms (left column) and their corresponding T_1 maps (right column) for PDCIS/EPC (P4), ADCIS (P5), phyllodes (P9), and IDC (P10). The lesions are drawn in red and appeared clearly hyperintense. Adipose and glandular tissues are drawn in blue and green respectively. The colourbar shows the T_1 in ms.

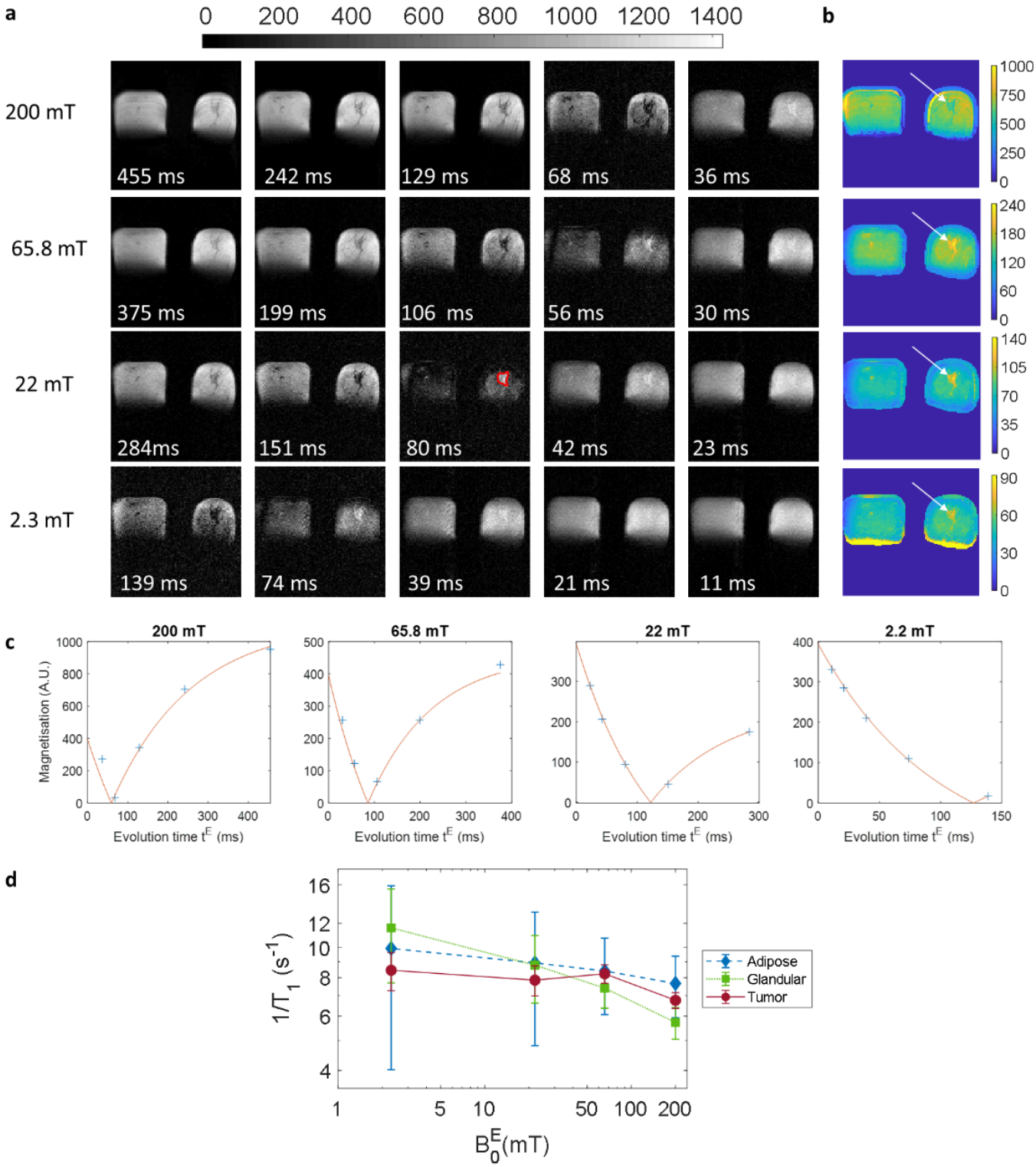

Figure 4

Example data from the typical patient P2 (ILC with DCIS grade 4). a) typical axial images showing the quality of our FCI prototype at the four B0E fields. Inside each image, the evolution time tE is given in ms. b) T1 maps at B0E= 2.3, 22, 65.8 and 200 mT. Heterogeneous T1 distribution throughout the breast is observed. The arrow shows the regions corresponding to the tumours (elevated values in yellow). The grey and colour bars show signal magnetization intensities in arbitrary unit (A.U) and T1 values in ms, respectively. P2 patient has a large breast that appear slightly square due to the restricted RF coil size. c) Magnetization relaxation recovery of tumour ROIs fitted using a monoexponential model in DCIS. The tumour ROI (in red colour) is depicted in image at B0E = 22 mT, tE= 80 ms. d) 1/T1-NMRD profiles from homogeneous ROIs of the DCIS, glandular and adipose tissues. The error bars are the fitting errors which were set equal to 1 sigma.

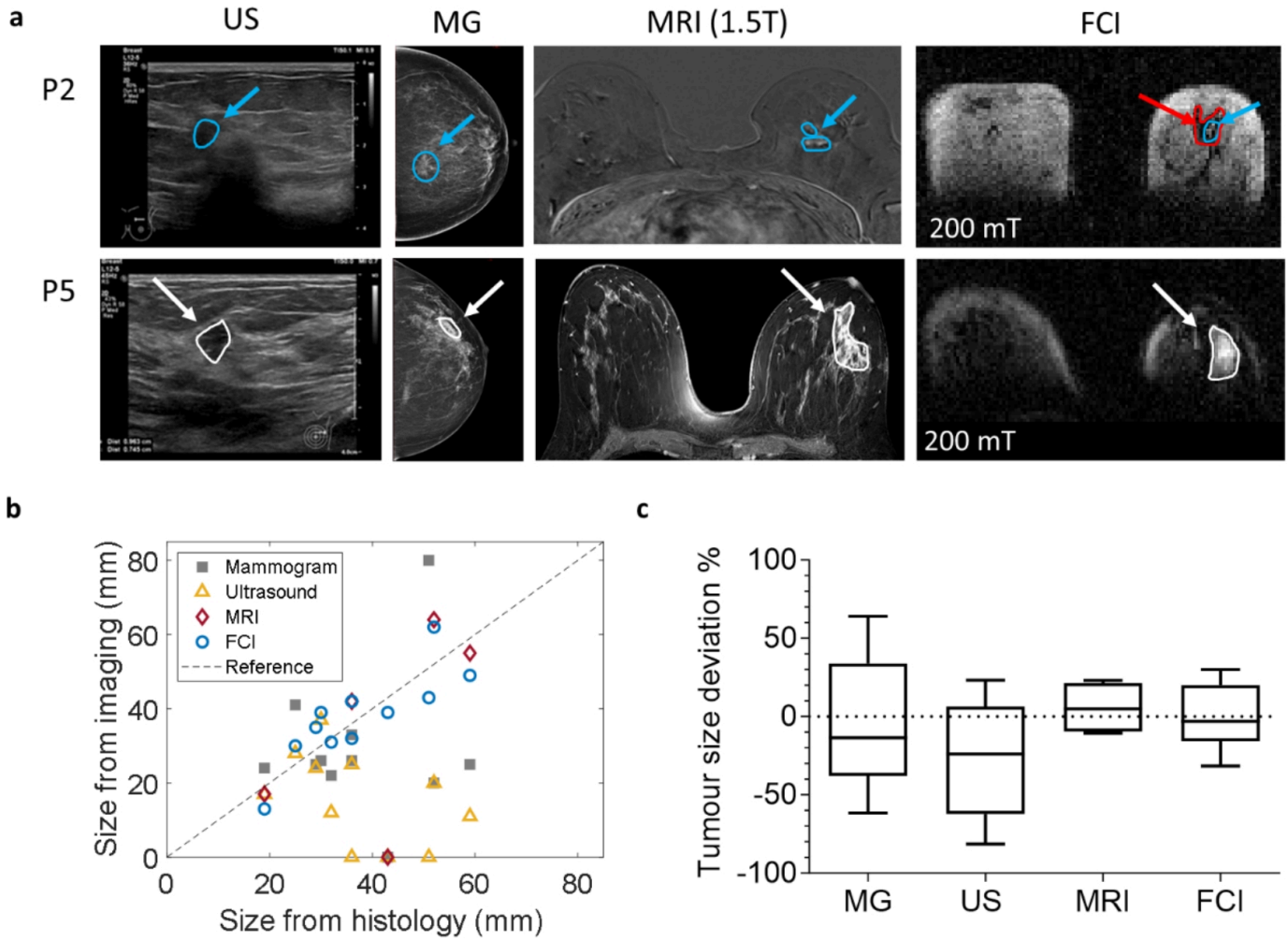

Figure 5

Tumour imaging visualisation and size measurements. **a)** US, MG, axial MRI and FCI images from patients P2 and P5. The ROIs show signal enhancement corresponding to the tumour areas. P2presented two distinct tumours in the left breast: ILC surrounded by DCIS. The ILC is detected by US and MG (blue ROI) and is shown as bright areas (blue ROIs indicated by blue arrows) in MRI. The DCIS is not seen in US, MG and MRI. FCI detected both lesions with bright area corresponding to ILC and dark area corresponding to DCIS as indicated by blue and red arrows respectively in FCI images (breast was squeezed due to the restricted RF coil size). For patient P5, the tumour is localised at the left breast and it is indicated by white arrows; For P5, the DCIS was not seen in MG but was retrospectively analysed to show a lesion of 25 mm. US showed a smaller mass of 11 mm (tumour in white ROI indicated by white arrows). **b)**Tumour size as measured by each imaging modality compared to the reference size obtained with HE-histology. NAD cases are also plotted. **c)** Tumour size deviation in MG, US, MRI from HE histology in %. FCI tumour sizes were closer to measurements from HE histology compared with US, MG and MRI (deviation = (imaging-HE histology)/HE histology x100).

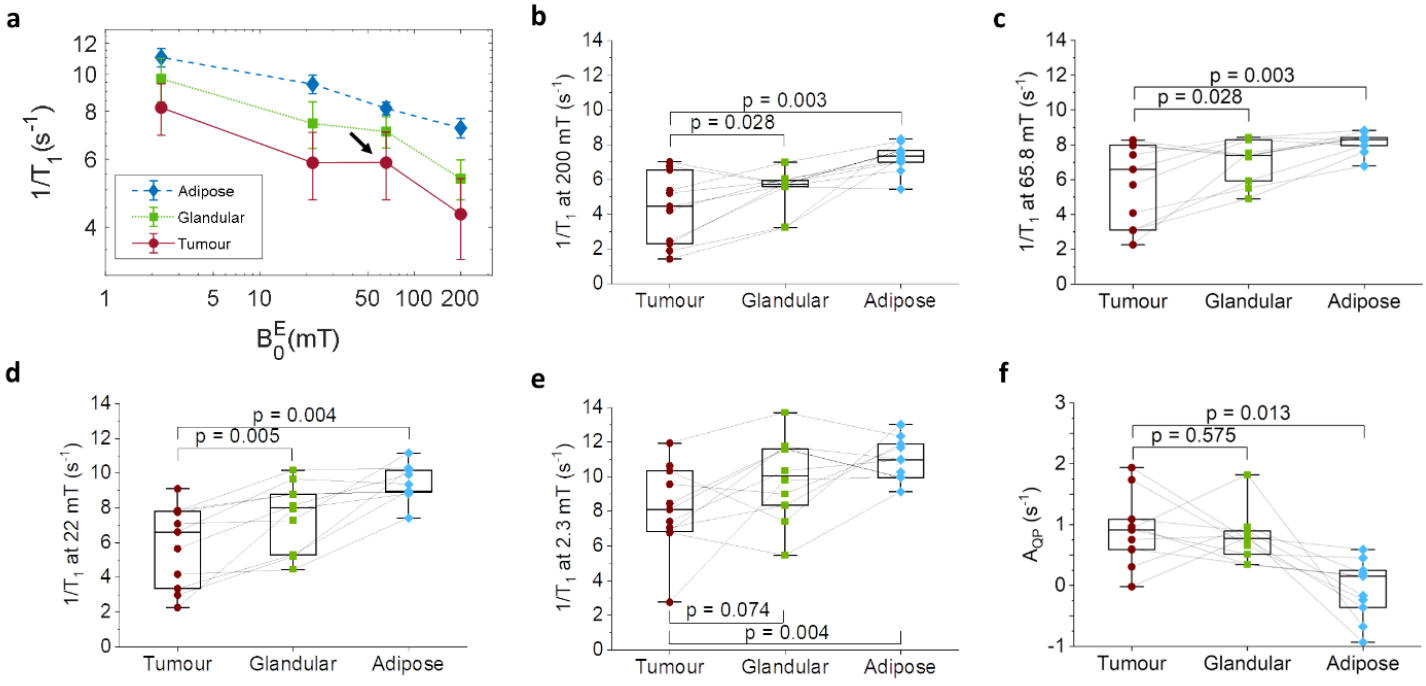

Figure 6

$1/T_1$-NMRD profiles and derived biomarkers for breast cancer detection. **a)** Average $1/T_1$-NMRD profiles for all the data (n = 11), obtained from the three ROIs shown in Figure 3: adipose tissues in blue, glandular tissues in green and tumour lesions in red. Clear trends can be observed between healthy and tumour tissues, despite the inter-patient variability (error bars, set to +/- sigma). The amplitude of QP peaks (arrow at data point at 65.8 mT) is clearly increased in tumours. **b-f)** Dot plots of the $1/T_1$ values at 200, 22, 2.3 mT and of the amplitude of the QP peak, showing significant differences between tumour and healthy tissues either glandular or adipose.

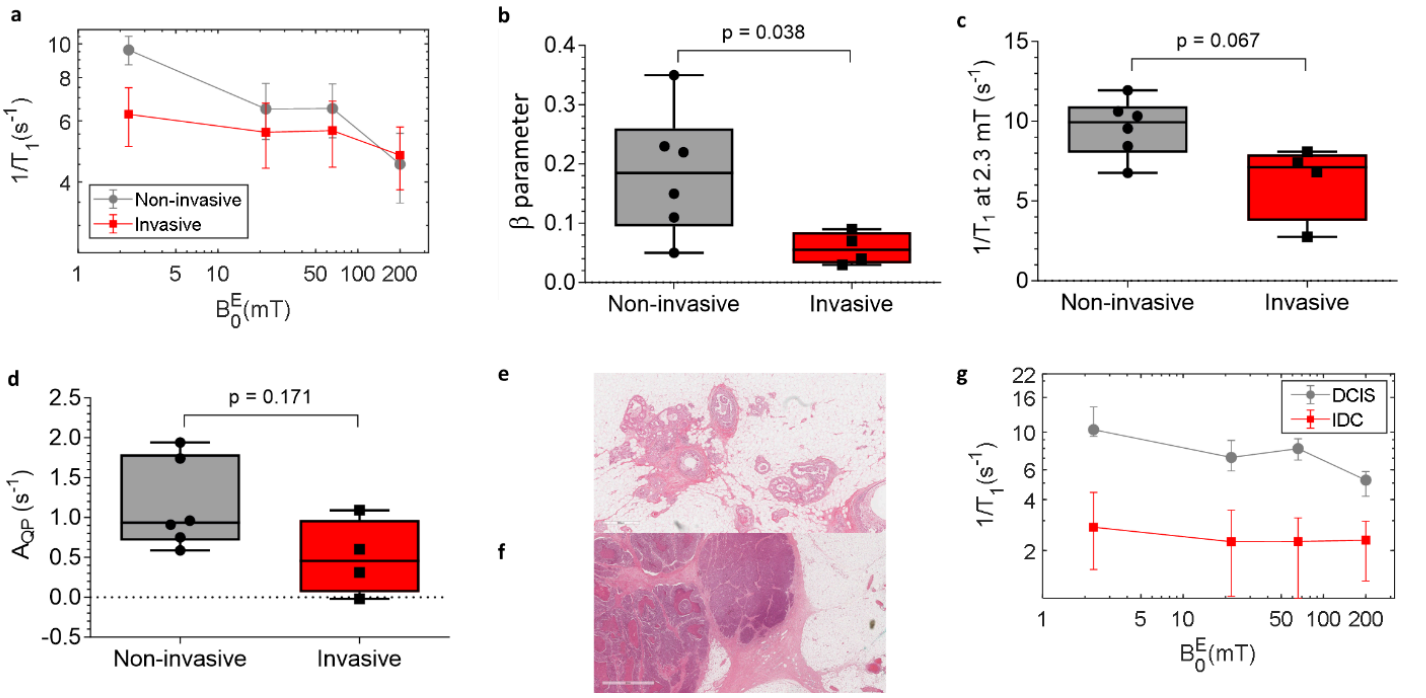

Figure 7

Comparison between Invasive and non-invasive tumours. Tumour dispersion profiles. **(a)** of invasive (red, n=4) (P2, P3, P6, P10) and non-invasive tumours (grey, n=6) (P1, P2, P4, P5, P7, P8), showing different behaviors of NMRD profiles (error bars were set to 1 sigma). Invasive tumours exhibited lower dispersion **(b)**, relaxation rate at 2.3 mT **(c)**, and lower QP peak amplitude **(d)**. **(e – f)** Representative HE histology

images of (non-invasive (DCIS, P8) and) invasive (IDC, P10) of breast tumour respectively. **(g)** Dispersion profiles of non-invasive (DCIS, P8, grey) and) invasive (IDC, P10, red).

Supplementary Files

This is a list of supplementary files associated with this preprint. Click to download.

- Supplement.docx